

The properties of 70 μ m-selected high-redshift galaxies in the Extended Groth Strip

M. Symeonidis^{1*}, S. P. Willner², D. Rigopoulou¹, J.-S. Huang², G. G. Fazio²
and M. J. Jarvis³

¹*Department of Astrophysics, University of Oxford, Denys Wilkinson Building, Keble Road, Oxford OX1 3RH, UK*

²*Harvard-Smithsonian Center for Astrophysics, 60 Garden street, Cambridge, MA 02138, USA*

³*Centre for Astrophysics, Science & Technology Research Institute, University of Hertfordshire, Hatfield AL10 9AB, UK*

Accepted 2007 December 21. Received 2007 December 20; in original form 2007 September 4

ABSTRACT

We examine the infrared properties of 43 high redshift ($0.1 < z < 1.2$), infrared-luminous galaxies in the Extended Groth Strip (EGS), selected by a deep 70 μ m survey with the Multiband Imaging Photometer on *Spitzer* (MIPS). In addition and with reference to starburst-type Spectral Energy Distributions (SEDs), we derive a set of equations for estimating the total infrared luminosity (L_{IR}) in the range 8–1000 μ m using photometry from at least one MIPS band. 42 out of 43 of our sources' optical/infrared SEDs ($\lambda_{observed} < 160 \mu$ m) are starburst-type, with only one object displaying a prominent power-law near-infrared continuum. For a quantitative analysis, models of radiation transfer in dusty media are fit onto the infrared photometry, revealing that the majority of galaxies are represented by high extinction, $A_v > 35$ and for a large fraction (~ 50 per cent) the SED turns over into the Rayleigh-Jeans regime at wavelengths longward of 90 μ m. For comparison, we also fit semi-empirical templates based on *local* galaxy data, however, these underestimate the far-infrared SED shape by a factor of at least 2 and in extreme cases up to 10 for the majority (~ 70 per cent) of the sources. Further investigation of SED characteristics reveals that the mid-infrared (70/24 μ m) continuum slope is decoupled from various galaxy properties such as the total infrared luminosity and far-infrared peak, quantified by the L_{160}/L_{70} ratio. In view of these results, we propose that these high-redshift galaxies have different properties to their local counterparts, in the sense that large amounts of dust cause heavy obscuration and are responsible for an additional cold emissive component, appearing as a *far-infrared excess* in their SEDs.

Key words: galaxies: general galaxies: high-redshift galaxies: starburst galaxies: photometry

1 INTRODUCTION

The classes of galaxies known as Luminous, Ultraluminous and Hyperluminous Infrared Galaxies (LIRGs, ULIRGs and HyLIRGs), have been a major subject of focus in observational cosmology since initial, groundbreaking studies such as those of Soifer et al. (1986) and Sanders et al. (1987). These objects, discovered in abundance by the Infrared Astronomical Satellite (*IRAS*), were found to possess an array of extreme properties, including an excessive energy output, effectively manifested as a large infrared/optical ratio (Sanders et al. 1989). It is now widely accepted that the combination of a powerful UV-photon source and the presence

of substantial amounts of dust are responsible for such extreme luminosities of the order of 10^{10} – $10^{14} L_{\odot}$ (e.g. Sanders & Mirabel 1996, Genzel et al. 1998). Determining the nature of the central energy source has been the subject of numerous subsequent studies, very often supplemented by multiwavelength data (e.g. Gregorich et al. 1995, Genzel et al. 1998, Rigopoulou et al. 1999, Klaas et al. 2001, Tacconi et al. 2002, Alonso-Herrero et al. 2005). These have revealed populations dominated by powerful starburst activity, but with a non-negligible Active Galactic Nucleus (AGN) contribution found to increase with bolometric luminosity (e.g. Veilleux et al. 1997, Tran et al. 2001, Brand et al. 2006).

The processes responsible for energy production and radiation transfer in the interstellar medium of such obscured systems are primarily evaluated by studying galaxy

* myrtos@astro.ox.ac.uk

Spectral Energy Distributions (SEDs), sometimes replacing spectroscopic diagnostics in determining the nature of the central engine. For infrared-luminous objects, these processes are greatly influenced by the composition, temperature and distribution of interstellar dust. Quantifying the infrared energy budget is, therefore, key in determining the generic properties of a galaxy and, as it is directly coupled to the central energy source, important in estimating the integrated cosmic star formation history. Cases where photometric data is scarce, benefit from various methods of data extrapolation and interpolation: construction of infrared SEDs has been a popular approach of modelling emission from dusty systems, either directly from first principles or semi-empirically, bridging together contributions from different parts of the interstellar medium (e.g. Guiderdoni et al. 1998, Calzetti et al. 2000, Rowan-Robinson 2000). Such models have enabled the examination of sources with extreme properties and pronounced infrared luminosity, either by solely considering star formation processes or including contribution from AGN. In addition, establishing correlations between monochromatic flux densities or luminosities has proven extremely advantageous and has conveniently been used as a first order approximation of the infrared energy budget, as well as a diagnostic for the physical processes in galaxies, adopted extensively in evolution studies (e.g. Franceschini et al. 2001).

In this paper we investigate the properties of 43 infrared-luminous galaxies from one of the first deep *Spitzer* far-IR surveys. This sub-sample is part of a population of 178 sources detected at $70\ \mu\text{m}$ by the Multiband Imaging Photometer on *Spitzer* (MIPS) (hereafter the $70\ \mu\text{m}$ population), down to a limiting flux density of $4\ \text{mJy}$ at 5σ . In Symeonidis et al. 2007 (hereafter S07), we gave a brief overview of the sources' properties and derived Star Formation Rate (SFR) estimates. Here, we aim to gain qualitative insight into their physical properties, primarily with respect to dust, comparing them to similar objects in the local universe. For this purpose and to quantitatively characterise the sample, we fit our photometry with three starburst dust models and a set of empirical local galaxy templates.

The paper is set out as follows: Section 2 introduces our selection criteria for the sub-sample, including an overview of infrared colours. Section 3 analyses and compares the model SED templates, associating the quality of fits to the properties of the sources. We investigate the infrared energy budget, with reference to SED characteristics such as the continuum slope and far-IR peak, in section 4. Finally, section 5 focuses on the derivation of a set of equations to calculate the total infrared luminosity in the range $8\text{--}1000\ \mu\text{m}$, with at least one MIPS band, for starburst-type sources. Our conclusions and discussion are presented in section 6. In all subsequent calculations, we have employed the following values: $H_o = 71\ \text{kms}^{-1}\text{Mpc}^{-1}$, $\Omega_M = 0.3$ and $\Omega_\Lambda = 0.7$.

2 INTRODUCING THE SAMPLE

2.1 Data sets and Selection Criteria

Our main data set is a $70\ \mu\text{m}$ image of the Extended Groth Strip (EGS) field, taken by MIPS. In this $\sim 0.5\ \text{deg}^2$ field, 178 sources were recovered down to a limiting flux density

of $4\ \text{mJy}$ at 5σ . We direct the reader to Davis et al. (2007) and S07 for a detailed description of all data sets acquired through the All-Wavelength Extended Groth Strip International Survey (AEGIS). In this section, we briefly refer to the Deep Extragalactic Evolutionary Probe 2 (DEEP2) spectroscopic survey, the *Spitzer* Infrared Array Camera (IRAC) survey and the MIPS survey.

70 and 90 per cent of the MIPS $70\ \mu\text{m}$ area is also covered by the IRAC survey and MIPS 24 and $160\ \mu\text{m}$ images, respectively. Within the overlap areas of all 8, 24 and $160\ \mu\text{m}$ images, we recover 100 per cent of our targets, a total of 122 sources (hereafter, the *full sample*). Of these, 103 also appear in the remaining three IRAC bands (3.6, 4.5 and $5.8\ \mu\text{m}$). DEEP2 obtained optical spectra for $\sim 14,000$ objects in the EGS with a limiting magnitude of $R_{AB} = 24.1$, using the DEIMOS spectrograph on the Keck telescopes (Davis et al. 2003). In the overlapping area (~ 75 per cent) between the MIPS $70\ \mu\text{m}$ image and the DEEP2 EGS survey, 43 reliable (quality factor ≥ 3) spectroscopic redshifts (z_{spec}) were retrieved in the range $0.1 < z < 1.2$, with a mean of 0.57 and a median of 0.51. For the remaining objects, some made the photometric cut but were assigned a poor quality redshift.

For the purpose of this work we select a sub-sample of the $70\ \mu\text{m}$ population (table 1) (hereafter, the *redshift sample*), which we require to be within the common area of the IRAC $8\ \mu\text{m}$ and the MIPS 24 and $160\ \mu\text{m}$ images, in order to sample the entire available infrared SED. The criteria are as follows:

- $8\ \mu\text{m}$ photometry from the IRAC survey
- 24 and $160\ \mu\text{m}$ photometry from the MIPS surveys
- a reliable spectroscopic redshift from DEEP2

It is the latter criterion which forms the basis of the selection, as the former two are always satisfied within the overlap regions. 34 objects in the redshift sample also appear in the 3.6, 4.5 and $5.8\ \mu\text{m}$ IRAC bands. The MIPS (24, 70 and $160\ \mu\text{m}$) colours of the redshift and full samples are similar (figure 1); apart from a few objects at the extremes of the 160/70 colour, for the majority of the population the received flux at $160\ \mu\text{m}$ is more than twice that at $70\ \mu\text{m}$ and shows no dependence on redshift or the strength of the $24\ \mu\text{m}$ mid-IR emission.

2.2 Spectral Energy Distributions

The SEDs of the 43 sources in the redshift sample are shown in figure 2. They are separated into three groups with respect to the total infrared luminosity in the $8\text{--}1000\ \mu\text{m}$ range — Starbursts ($10^{10} - 10^{11} L_\odot$), LIRGs ($10^{11}\text{--}10^{12} L_\odot$) and ULIRGs ($10^{12} - 10^{13} L_\odot$) (see section 4). The SED of an object which displays a clear power-law near-IR continuum is in black. This was eliminated through examination of IRAC colours commonly used to identify objects whose SED is AGN-dominated (e.g. Lacy et al. 2004, Stern et al. 2005).

An obvious trend in the SEDs is the reduction of the stellar bump with respect to the infrared continuum, for objects of increasing luminosity and, as this is a flux limited survey, redshift. A similar observation was made by Alonso-Herrero et al. (2006), who found the stellar bump greatly reduced or completely wiped out in local ULIRGs. This could be a direct consequence of an increasing AGN versus starburst dominance, indicating the tendency towards a power-

Table 1. The redshift sample (43 sources) - Object cardinal numbers with the prefix EGS70 referring to the 70 μ m EGS survey, coordinates, spectroscopic redshifts, R-band magnitudes (AB), measured flux densities at 24, 70 and 160 μ m. The MIPS 24 μ m calibration uncertainty is 10 per cent, whereas for MIPS 70 and 160 μ m it is 20 and 30 per cent, respectively.

ID	ra (J2000) h m s	dec (J2000) deg min arc	z_{spec}	R mag (AB)	f_{24} (mJy)	f_{70} (mJy)	f_{160} (mJy)
EGS70-41	14 24 26.1	+53 37 23.0	0.45	20.9	1.3	44.1	117.6
EGS70-51	14 24 34.3	+53 36 05.4	0.22	18.6	0.9	6.9	29.1
EGS70-55	14 24 28.2	+53 36 44.6	0.67	21.6	0.6	16.9	60.0
EGS70-58	14 25 02.8	+53 31 25.5	0.69	22.3	0.3	10.4	115.2
EGS70-67	14 24 30.1	+53 35 42.9	0.96	22.1	1.0	11.6	85.7
EGS70-70	14 24 41.5	+53 33 43.2	0.78	21.3	0.46	14.6	104.5
EGS70-72	14 24 55.0	+53 30 04.6	0.39	20.4	0.76	11.8	23.0
EGS70-76	14 24 29.6	+53 31 21.3	0.73	22.6	0.11	10.5	10.2
EGS70-77	14 23 43.1	+53 35 06.1	0.42	19.2	1.4	22.3	148.8
EGS70-78	14 24 08.2	+53 31 22.3	0.37	20.3	1.0	15.5	57.2
EGS70-82	14 23 49.6	+53 31 35.4	1.03	23.4	0.38	21.7	64.3
EGS70-84	14 23 48.8	+53 30 09.0	0.77	22.0	0.99	13.9	99.3
EGS70-85	14 24 01.2	+53 27 54.4	0.43	19.9	0.95	12.0	38.1
EGS70-88	14 23 49.4	+53 26 29.8	0.78	21.5	1.68	40.0	111.5
EGS70-93	14 23 16.1	+53 30 47.4	1.2	22.6	0.69	14.1	130.5
EGS70-94	14 23 30.9	+53 28 22.5	1.02	21.7	0.67	11.5	82.5
EGS70-98	14 23 35.4	+53 26 12.3	0.29	20.1	1.85	14.9	48.3
EGS70-100	14 23 31.6	+53 26 25.1	0.3	19.3	2.5	35.9	68.7
EGS70-103	14 23 39.6	+53 22 32.0	0.25	19.0	0.9	12.9	60.6
EGS70-110	14 23 18.2	+53 24 53.5	0.42	21.3	0.5	30.5	48.6
EGS70-114	14 23 01.6	+53 24 20.7	0.66	20.8	1.1	16.6	76.8
EGS70-115	14 23 12.7	+53 22 16.0	0.38	20.1	1.2	14.2	57.5
EGS70-120	14 23 22.8	+53 19 29.2	0.57	21.6	0.5	8.9	25.8
EGS70-121	14 23 00.1	+53 21 51.9	0.78	22.1	0.7	7.7	25.2
EGS70-122	14 22 50.0	+53 22 53.3	0.28	19.4	1.0	14.6	74.1
EGS70-124	14 22 39.1	+53 24 20.3	0.85	21.3	1.1	13.9	61.1
EGS70-125	14 22 47.3	+53 22 20.2	0.25	20.7	0.7	11.3	44.5
EGS70-126	14 23 14.7	+53 17 59.5	0.42	21.2	0.6	29.5	41.4
EGS70-134	14 22 56.3	+53 17 10.1	0.75	21.9	0.4	4.8	46.2
EGS70-137	14 23 05.7	+53 15 28.1	0.48	20.1	0.75	14.4	103.5
EGS70-138	14 22 22.3	+53 21 58.2	0.42	21.1	0.26	7.5	32.5
EGS70-140	14 22 25.4	+53 20 30.0	0.46	19.4	0.57	10.7	43.8
EGS70-141	14 22 11.8	+53 19 50.0	0.70	22.7	0.54	11.4	7.3
EGS70-144	14 22 36.8	+53 15 01.1	0.19	19.3	0.75	13.0	37.0
EGS70-146	14 22 18.1	+53 16 43.6	0.46	20.1	0.64	8.9	28.5
EGS70-147	14 21 54.3	+53 19 51.4	0.67	22.3	0.49	8.8	44.2
EGS70-149	14 22 21.1	+53 14 33.9	0.51	20.3	0.69	14.	64.6
EGS70-150	14 21 55.4	+53 18 10.4	0.74	22.0	0.71	6.1	22.1
EGS70-152	14 22 31.1	+53 12 37.5	0.37	20.0	0.98	13.1	124.4
EGS70-155	14 22 17.7	+53 14 32.7	0.17	18.6	1.2	16.7	11.2
EGS70-158	14 21 37.5	+53 17 17.8	0.93	22.1	1.4	30.2	143.4
EGS70-165	14 21 55.9	+53 14 22.1	0.77	21.7	2.8	16.7	28.0
EGS70-172	14 21 41.1	+53 15 03.8	0.48	23.1	0.2	13.2	85.7

law near-IR continuum or simply due to the fact that the more infrared-luminous galaxies will be fainter in the optical because of increased extinction. For the lower-redshift objects, the 6.2 and/or 7.7 μ m PAH features are redshifted into the 8 μ m band, which displays a clear increase in flux. Contrary to the pronounced differences in the near-IR, the mid/far-IR (24-160 μ m) part of the SEDs makes them indistinguishable; this has also been noted by other authors, e.g. Klaas et al. (2001) and it is potentially indicative of the fact that far-IR emission is independent from the nature of the central energy source.

3 SED FITTING

In past years, there have been numerous efforts to characterise and reproduce galaxy SEDs with model templates (e.g. Rowan-Robinson 1980, 1995, Appleton et al. 2004). These have been developed either semi-empirically or by applying detailed radiation transfer calculations; in either case there has been reasonable success with respect to the models' representation of real systems (e.g. Efstathiou & Rowan-Robinson 1990, Granato 1994, Silva 1998, Rowan-Robinson et al. 2005, Efstathiou, Rowan-Robinson & Siebenmorgen 2003, Siebenmorgen & Krügel 2007). Our motive for SED fitting is to determine the infrared energy budget of each source and gain insight into its physical properties. Since the redshift sample mostly displays SEDs typical of starburst

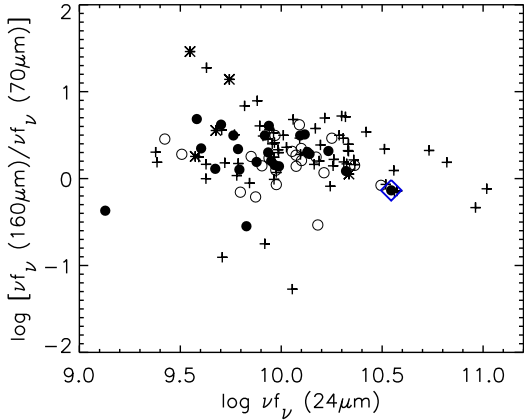


Figure 1. Infrared colours for the full sample - ratio of $160 \mu\text{m}$ νf_ν to $70 \mu\text{m}$ νf_ν versus $24 \mu\text{m}$ νf_ν . Asterisks represent $R > 24.1$ sources with no z_{spec} , while the rest of the symbols are divided into $z \leq 0.5$ (empty circles), $z > 0.5$ (filled circles) and $R < 24.1$ sources with no z_{spec} (crosses). The blue diamond symbol corresponds to the object we identified as AGN-dominated (see discussion in section 2.2).

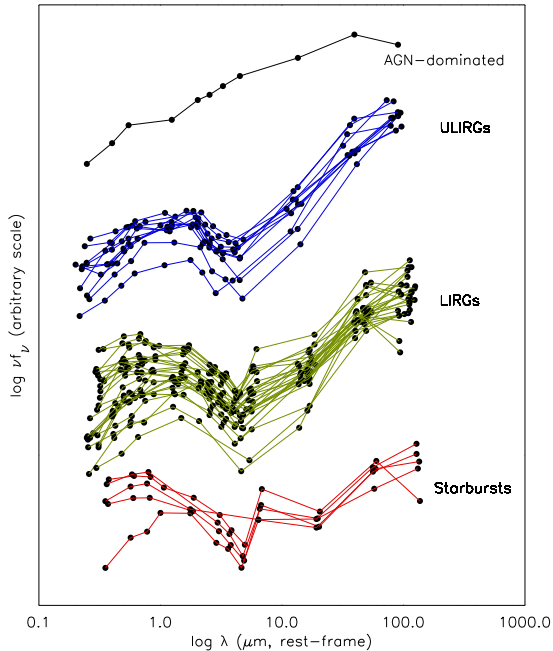


Figure 2. The optical to far-IR SEDs of the 43 objects in the redshift sample. They are split into 3 luminosity classes - Starbursts (red), LIRGs (green) and ULIRGs (blue). Due to the flux density limits of the $70 \mu\text{m}$ survey, an increase in total infrared luminosity corresponds to increasing redshift, with all starbursts at $z \leq 0.25$ and all ULIRGs at $z \geq 0.65$. The AGN-dominated SED (see section 2.2) is shown in black. The photometry (*BRIJK*, 3.6, 4.5, 5.8, 8, 24, 70 and $160 \mu\text{m}$) is redshift-corrected.

galaxies, we require models of radiative transfer through dusty media, considering solely starburst processes. Accordingly, object 165, whose SED we evaluate as AGN-dominated (see section 2.2), is not included in our analysis. Nevertheless, we do not exclude a strong AGN contribution in the remaining galaxies. Simply, at this stage, due to the extremely obscured nature of these objects, we cannot reach any further conclusions without exploring their multiwavelength properties, which is beyond the scope of this paper.

We use the Chary & Elbaz (2001, hereafter CE01), Dale & Helou (2002, hereafter DH02) and Siebenmorgen & Krügel (2007, hereafter SK07) libraries, selected on account of their diverse frameworks and the fact that they span a wide range in infrared luminosity ($10^9 - 10^{14} L_\odot$), from star-forming galaxies to HyLIRGs. In subsection 3.1 we touch upon the main characteristics of the models that are relevant to our study. For a more detailed report, we refer the reader to the relevant papers.

3.1 The dust models

The CE01 SED templates are based on the models of Silva et al. (1998, hereafter S98). S98 employ a stellar population synthesis framework, using Simple Stellar populations (SSP) of different age and metallicity, including circumstellar dust shells/outflows of AGB stars that continuously enrich the ISM. Two types of environments are responsible for the infrared continuum - dust emission associated with star-forming molecular clouds and a cirrus component associated with the intensity of the stellar field. CE01 generate template SEDs, in the UV-submm range, of four prototypical galaxies, Arp 220, NGC 6090, M82, and M51, corresponding to four luminosity classes: ULIRGs, LIRGs, starbursts and normal galaxies. They partition the four SEDs into mid and far-infrared components and interpolate between them to create a set of templates with a range of luminosities, from which they select the ones which correspond to observed ranges of *IRAS* and Infrared Space Observatory (*ISO*) colours.

The DH02 templates are based on the work of Desert, Boulanger & Puget (1990, hereafter DBP90). DBP90 introduce an empirical model combining emission from Very Large Grains (VLGs) in thermal equilibrium, stochastically heated Very Small Grains (VSGs) and Polycyclic Aromatic Hydrocarbon (PAH) features, in radiation fields of varying intensity. DH02 produce a set of semi-empirical infrared SEDs, the shape of which is determined by the intensity U of the interstellar radiation field. They develop a power law dependence of the dust mass on the value of U , the outcome of which is a collection of dusty environments immersed in a range of radiation fields, representing a mixture of active and quiescent regions. Their SEDs are further constrained by *IRAS* and *ISO* observations of local star-forming galaxies with L_{IR} ranging from 10^8 to $10^{12} L_\odot$. In addition they vary the emissivity index β , which relates the emissivity of dust grains to the wavelength of emission.

The SK07 model SEDs are built on the formulation of Krügel & Siebenmorgen (1994), who present a modified definition of a starburst nucleus: instead of a central radiating point source, they employ a configuration where stars are distributed throughout the volume, introducing ‘Hot Spots’ - dust regions enveloping OB stars. Correspondingly, in their calculations, the dust temperature is varied both in the lo-

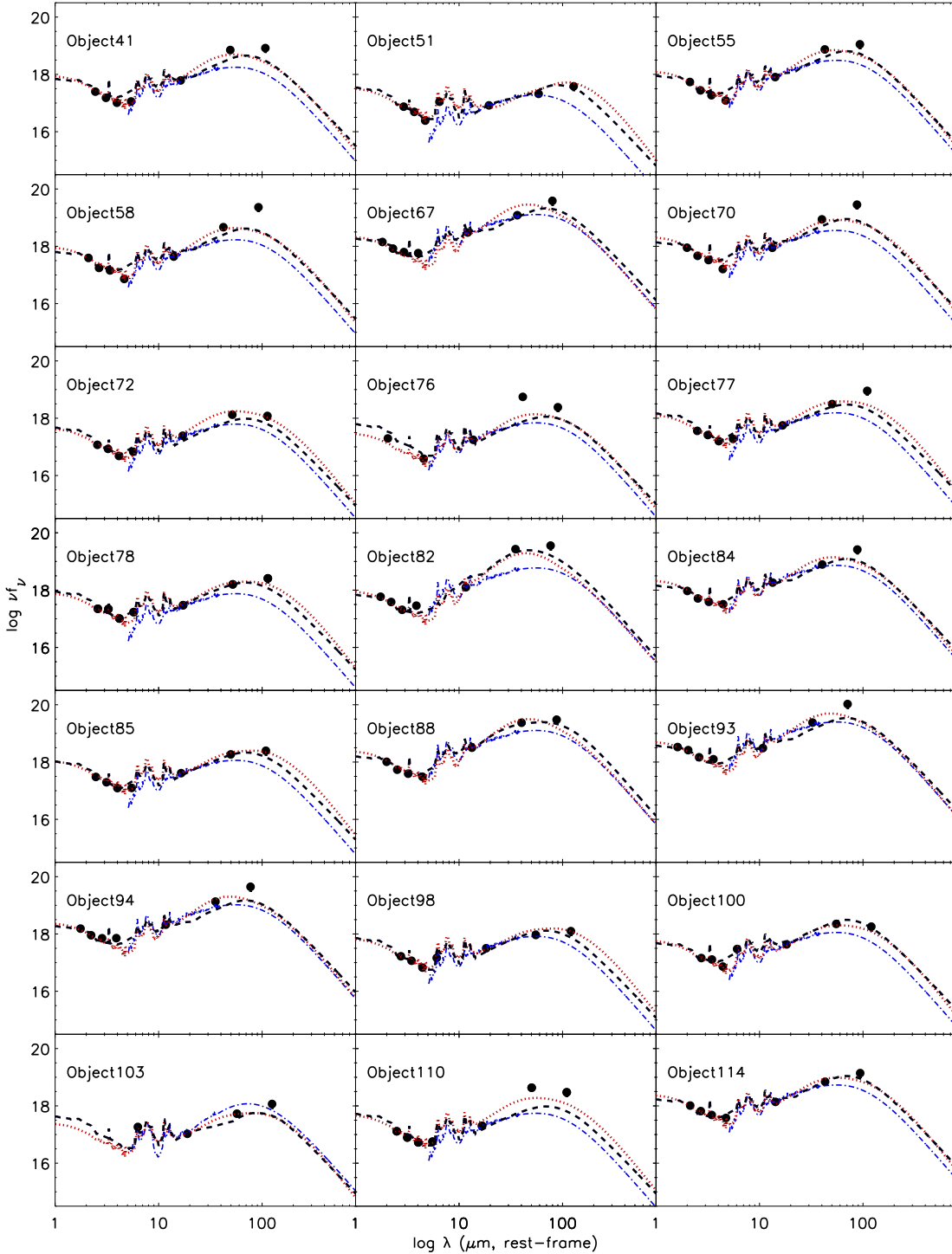


Figure 3. SEDs for the first 21 objects from the redshift sample fitted with the CE01 (black dashed curve), DH02 (red dotted curve) and our empirical templates (blue dot-dashed curve). Only the best-matched (lowest χ^2) template is shown. The filled circles are Spitzer broadband data for the redshift sample, including calibration errors of 10 per cent for the IRAC and MIPS $24\mu\text{m}$ photometry, 20 per cent for MIPS $70\mu\text{m}$ and 30 per cent for MIPS $160\mu\text{m}$. All photometry has been colour-corrected and redshift-corrected so the plots are at $z\sim 0$.

cality of each star as well as with distance from the nucleus. Furthermore, since part of the stellar flux is absorbed within the hot spot and re-radiated in the IR, their formulation replaces some OB stars by IR-emitting hot spots. This has the effect of reducing the overall temperature, whilst keep-

ing mid-IR emission unchanged, as this is considered to be linked to the density of dust within the hot spot. All other stars are treated separately and are assumed to contribute to the far-IR part, ‘cirrus’ component of the SED. Their library of ~ 7000 templates ranges in 5 free parameters, in

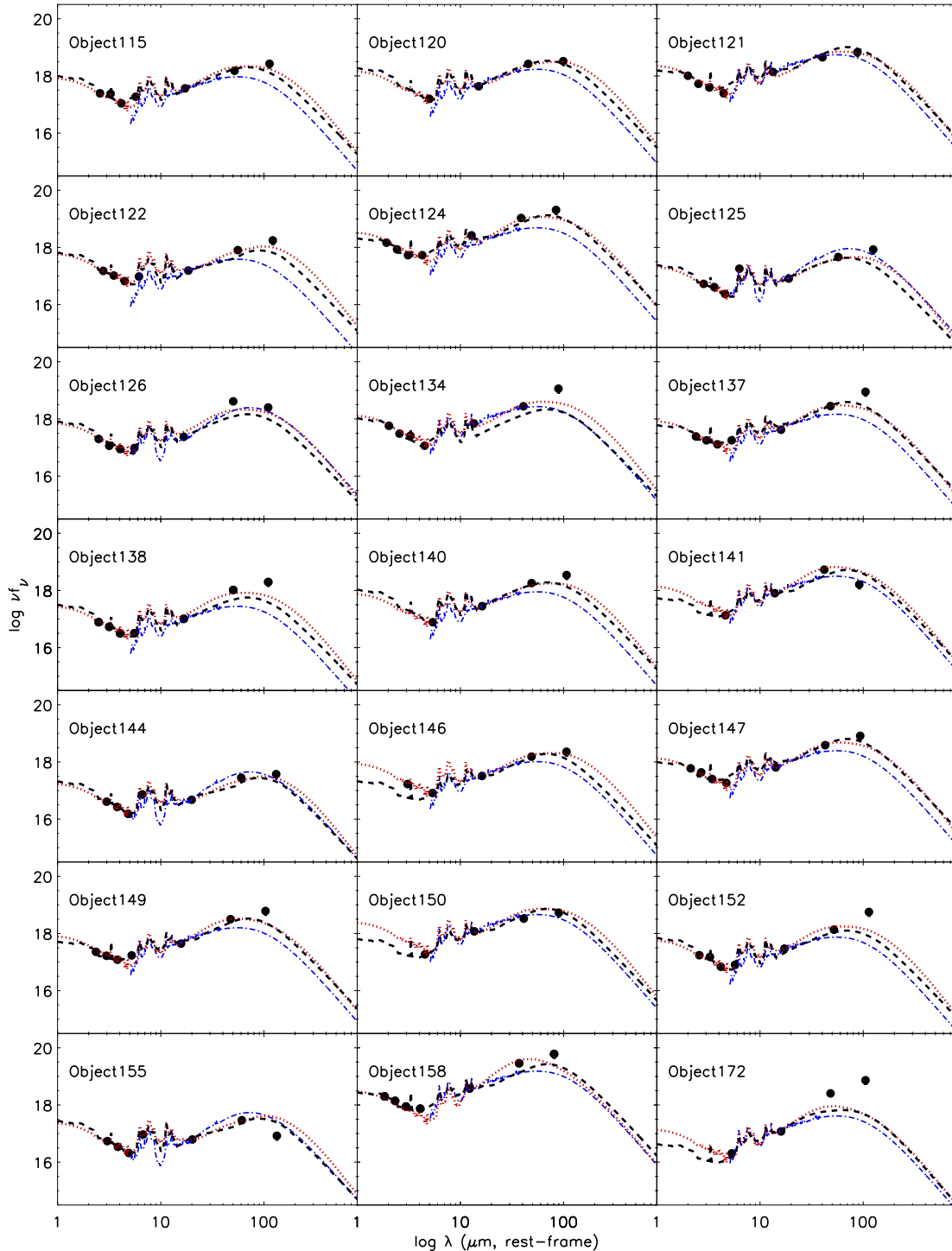


Figure 4. SEDs for the remaining 21 objects from the redshift sample fitted with the CE01 (black dashed curve), DH02 (red dotted curve) and our empirical templates (blue dot-dashed curve). Only the best-matched (lowest χ^2) template is shown. The filled circles are Spitzer broadband data for the redshift sample, including calibration errors of 10 per cent for the IRAC and MIPS 24 μm photometry, 20 per cent for MIPS 70 μm and 30 per cent for MIPS 160 μm . All photometry has been colour-corrected and redshift-corrected so the plots are at $z \sim 0$.

physically acceptable combinations: radius of dust emitting region, total luminosity, visual extinction and hot spot dust density. The fifth parameter, L_{OB}/L_{tot} , represents the percentage of the total infrared luminosity that originates from OB stars, compared to the contribution from the general

stellar population and a result it has a direct effect on the near-IR flux and the representation of the near-IR stellar bump.

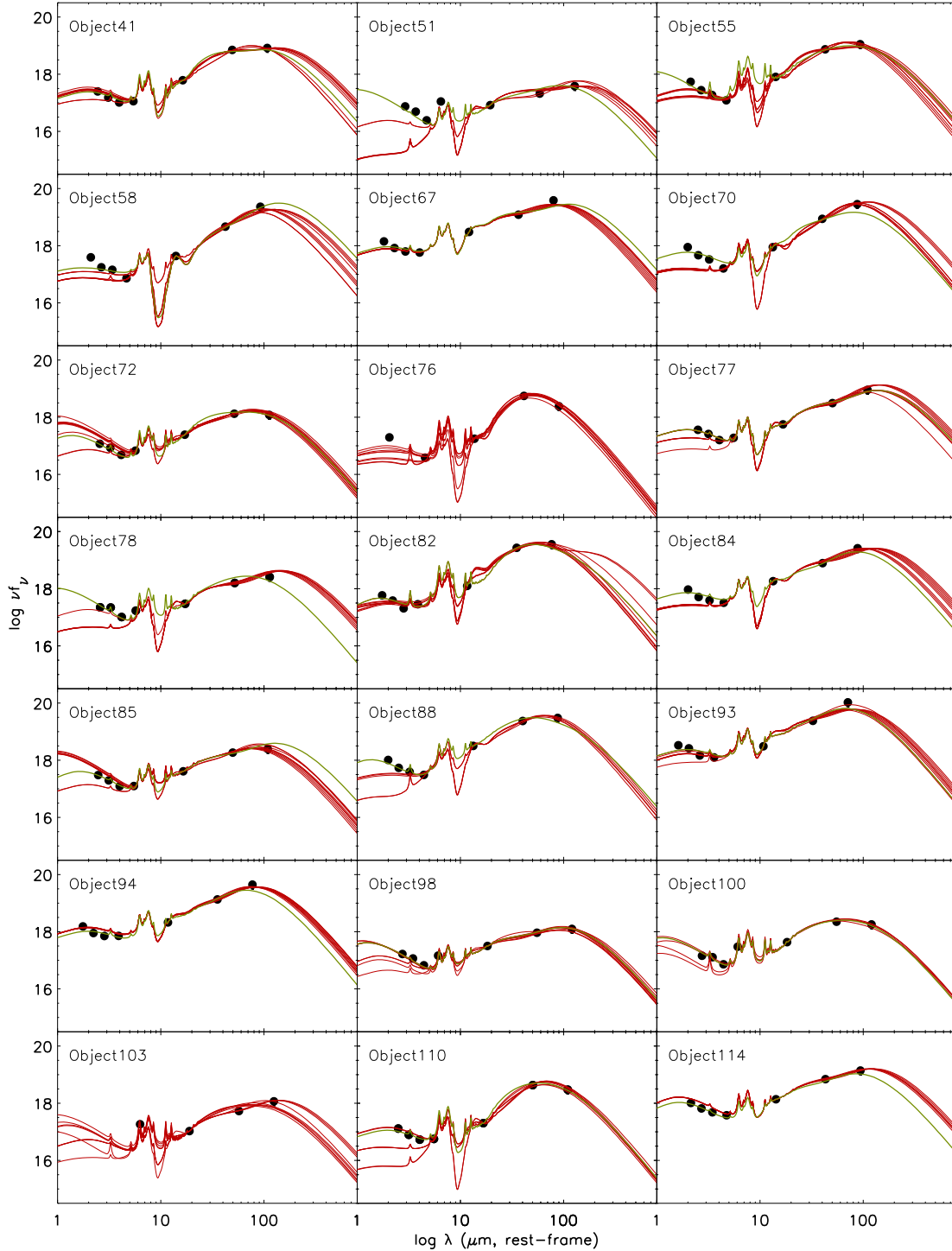


Figure 5. SEDs for the first 21 objects from the redshift sample fitted with the SK07 templates. The red curves represent the matches with the lowest χ^2 values (see section 3.3), fitted on 8, 24, 70 and $160\mu\text{m}$ photometry. The green curve represents the match with the lowest χ^2 value when fitted on 3.6, 4.5, 5.8, 8, 24, 70 and $160\mu\text{m}$ photometry. The filled circles are Spitzer broadband data for the redshift sample, including calibration errors of 10 per cent for the IRAC and MIPS $24\mu\text{m}$ photometry, 20 per cent for MIPS $70\mu\text{m}$ and 30 per cent for MIPS $160\mu\text{m}$. All photometry has been colour-corrected and redshift-corrected so the plots are at $z\sim 0$.

3.2 Our empirical templates

In addition to the models and as a consistency check, we fit a set of real galaxy templates, which we construct by combining spectral and photometric data of local star-

bursts. The templates are built on a collection of mid-IR (5– $38\mu\text{m}$) *Spitzer* InfraRed Spectrograph (IRS) spectra (courtesy of Brandl et al. 2006) from the central region of 16 local Starbursts, as well as *IRAS* broadband data (12, 25, 60 and $100\mu\text{m}$) from the NASA Extragalactic Database

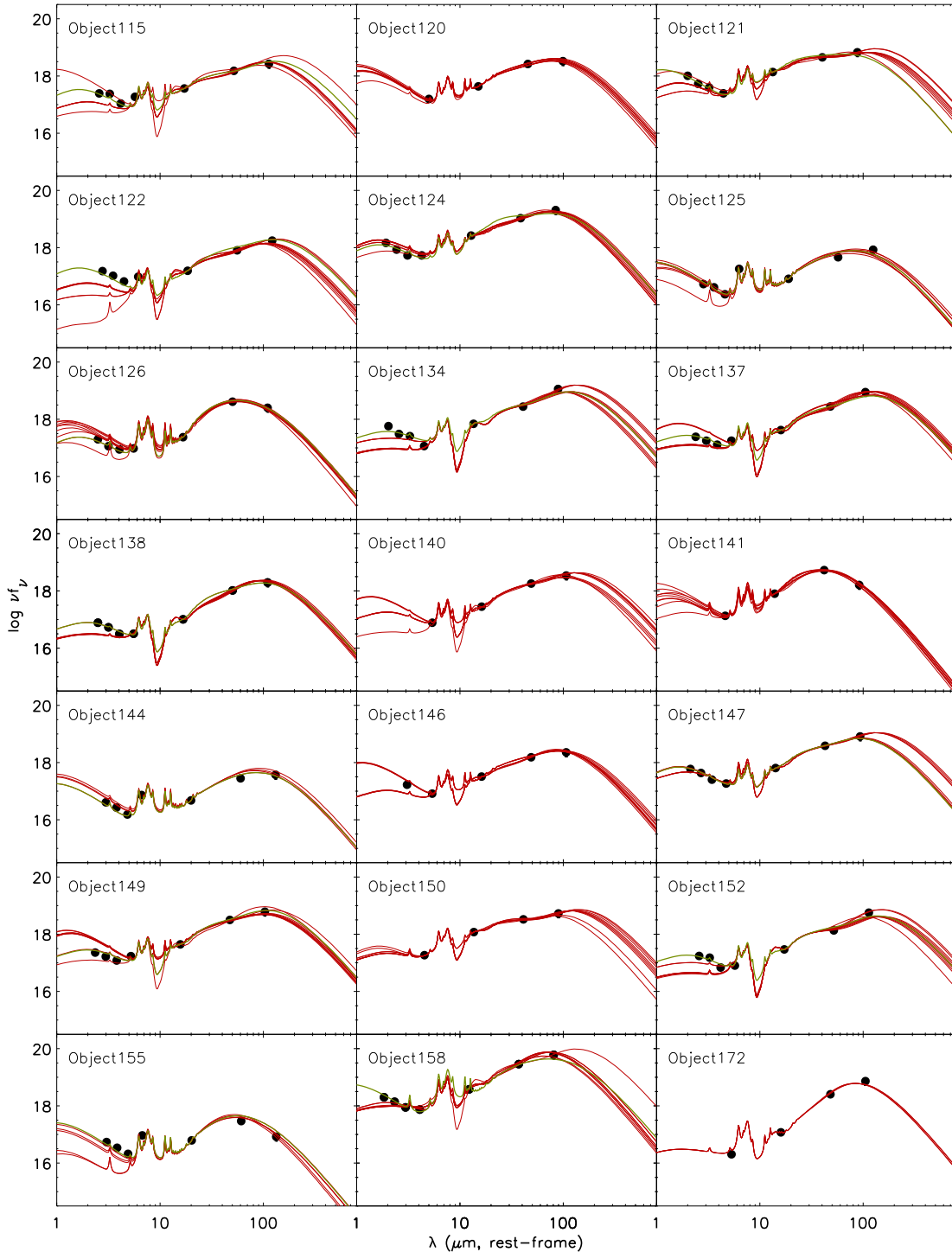


Figure 6. SEDs for the remaining 21 objects from the redshift sample fitted with the SK07 templates. The red curves represent the matches with the lowest χ^2 values (see section 3.3), fitted on 8, 24, 70 and 160 μm photometry. The green curve represents the match with the lowest χ^2 value when fitted on 3.6, 4.5, 5.8, 8, 24, 70 and 160 μm photometry. The filled circles are Spitzer broadband data for the redshift sample, including calibration errors of 10 per cent for the IRAC and MIPS 24 μm photometry, 20 per cent for MIPS 70 μm and 30 per cent for MIPS 160 μm . All photometry has been colour-corrected and redshift-corrected so the plots are at $z \sim 0$.

(NED). The far-IR/submm region (longward of 60 μm) is fitted with a modified black-body emission law, as it is considered to sample emission from cool dust in equilibrium heated by the interstellar medium. This is of the form $B_\lambda(T)(1 - e^{-\tau_\lambda})$, with a wavelength dependent optical depth

$\tau_\lambda = \tau_{100\mu\text{m}}(100\mu\text{m}/\lambda)^\beta$ (e.g. see Klaas et al. 2001) and a dust emissivity index β . We assume a low opacity limit, so approximate the term $(1 - e^{-\tau_\lambda})$ by $\lambda^{-\beta}$. Typical reported values of β range between 1.5–2 (e.g. Dunne et al. 2000, Lisenfeld, Isaak & Hills 2000), so we adopt $\beta=1.5$, consistent

with studies of the far-IR emissivity of large grains (Desert, Boulanger & Puget 1990). The greybody temperature is allowed to vary in order to minimise χ^2 on the 60–100 μ m region, resulting in a temperature range of 30–50 K. These 16 empirical SED templates vary with respect to total infrared luminosity, position of far-IR peak and mid-IR continuum slope.

3.3 Model Comparison

The best (lowest χ^2) SED matches for the redshift sample are shown in figures 3–6. All photometry has been colour-corrected according to the specifications in the IRAC and MIPS data handbooks. With the CE01 and DH02 SEDs we use all available IRAC photometry and the three MIPS bands. In the case of our empirical SEDs, only the 8–160 μ m region is taken into account, because the templates do not extend to short wavelengths. The SK07 models do not treat the near-IR emission in detail, so the fits are approached in two ways: we fit the 3.6–160 μ m region (where IRAC photometry is available) and the 8–160 μ m region separately. For the latter all matches with similarly low χ^2 values are kept, in order to increase the accuracy of the results, since the library contains ~ 7000 SEDs and limiting the number of photometric points for the χ^2 , dramatically reduces the constraints on the chosen templates. Furthermore, near-IR photometry is fit with slightly increased errors in order to take into account the weakness of the models in that region.

In the mid-IR ($\lambda_{rest} < 40 \mu$ m) all templates deliver the emission/absorption lines and continuum slope with the same consistency; in some cases the 8 μ m colour-corrected flux samples a PAH feature (e.g. objects 98, 100, 103, 122, 125). However, there are large discrepancies in the 10 μ m silicate absorption depth. For the CE01 and DH02 templates it seems to vary over a small range; this is not the case for the SK07 SEDs, where it can be 50–100 times below the continuum (e.g. see objects 58, 70, 76, 82, 110). This is a direct consequence of SK07 incorporating dust self-absorption in their models, an effect assigned to increasing quantities of dust at low temperatures (e.g. Mitchell & Robinson 1981), resulting in an overall shift of the far-IR peak to longer wavelengths. Our photometry misses the silicate feature so we cannot constrain its depth, nevertheless its varied strength in the models is consistent with observations as it is commonly found in LIRG & ULIRG spectra (e.g. Hao et al. 2007, Armus et al. 2007) and its existence is correlated with the magnitude of extinction.

The differences between the templates are more striking in the far-IR ($\lambda_{rest} > 40 \mu$ m). The SK07 models are in good agreement with the data. In addition, most 3.6–160 μ m fits result in templates with similar characteristics to the 8–160 μ m fits, showing that the far-IR is well constrained even without the $< 6 \mu$ m region. On the contrary, DH02 and CE01 often underproduce the 160 μ m flux, by an amount significantly higher than the 30 per cent photometric uncertainty and up to a factor of 10 in extreme cases (e.g. see objects 58, 70, 84, 93, 94, 110, 134, 137, 138, 152, 172 for which the effect is more exaggerated). Moreover, it is worth noting that most objects for which the far-IR is completely underestimated by CE01 and DH02, have a ratio of $L_{70}/L_{24} > 3.4$ (table 3), suggesting that a steep mid-IR continuum and

a high far-IR flux are contradictory features in these templates.

Table 2 shows the parameters generated from the best matched SK07 templates. The nuclear radius represents the region of total dust emission from the entire stellar population, with the OB stars only confined to the inner 350pc. The majority of best fit models are described by a radius of 3kpc, suggesting emission from extended regions of cool dust. In terms of visual extinction, the matches span the whole available range of $2 < A_v < 144$. Taking into account the variations of A_v for each object with respect to each template, it is worth noting that only 5 out of 42 galaxies are matched solely with $A_v < 10$ templates, the remaining appearing mostly with $A_v \sim 35$ or 70, implying high obscuration in these systems. Finally, the value of hot spot dust density, which is directly related to the strength of mid-IR emission appears to have a wide range in values, but in most objects it reaches the maximum of $\rho = 10000 \text{ cm}^{-3}$.

3.4 Summary

For the 8–160 μ m region, the SK07 models provide the best matches to our sources' infrared SEDs. The fact that the CE01 and DH02 templates in most cases severely underestimate the far-IR, leads us to two conclusions. Firstly, the notion of a single radiating source is an over-simplification of a real system, which is more likely to be a complex and clumpy 3-D configuration with a varying temperature gradient. Secondly, we propose that these high-z objects have higher obscuration and additional far-IR emission from a cold dust component that is not commonly seen in local LIRGs/ULIRGs, on which the CE01 and DH02 templates are based. Such excess far-IR flux would be a direct consequence of a large emitting dust region, where dust in the immediate vicinity of young stars (and/or an AGN), would be responsible for greatly attenuating the radiation field and hence shielding the outer dust layers from direct UV illumination, resulting in lower equilibrium temperatures. This scenario is well-expressed by the SK07 models; by including the treatment of hot spots around OB stars, the average dust temperature is lowered, shifting the far-IR peak to longer wavelengths, without a reduction in the mid-IR flux, which, according to their framework, is only linked to the dust density in the hot spot. In contrast, the CE01 and DH02 templates, which have been found to work well with local sources, fail in this case, because their formulation does not allow for the possibility of excess far-IR flux independent from the mid-IR. These observations are further supported by our empirical SED fits, which were included for the purpose of comparing with real local galaxy data (see section 3.2). The majority show considerable discrepancies, failing to reproduce the far-IR SED shape (e.g. objects 77, 93, 110, 122), indicating that the greybody temperatures of 30–50 K are too high and that dust potentially colder than 30 K is present in most systems.

In view of these results, our subsequent calculations consider only the SK07 fits to the 8–160 μ m spectral region. The fact that the near-IR part of the SED is not well-represented, is not important since we are only concerned with pure dust emission in the 8–1000 μ m range. For each object, we take into account all SK07 matches (figures 5 and 6 and table 2), to establish a valid error margin in cases

Table 2. Parameters corresponding to the SK07 templates, fitted with photometry at 8, 24, 70 and 160 μm , that produced the lowest χ^2 matches (used in subsequent calculations). The columns are as follows: Object ID, radius of the central nuclear region (kpc), ratio of the luminosity from OB stars to the total luminosity (L_{OB}/L_{tot}), total visual extinction measured from the surface to the centre of the starburst (A_v) and density within the hot spots ρ (cm^{-3}). Where a range is quoted, e.g. $\rho=100\text{--}10000$, each of the matched models came up with a value of ρ between those limits. Where there is a coma, e.g. 100, 10000, each of the matched models had either ρ of 100 or 10000, but not in between.

ID	Nuclear radius (kpc)	L_{OB}/L_{tot} (%)	A_v	ρ (cm^{-3})
41	0.35,3	40,60	35.9,72	100–5000
51	3	40,90	35.9,67.3	10000
55	0.35,3	40,60	35.9,72	100–10000
58	0.35,1,3	40,60	119,144	5000,10000
67	1,3	60	35.4,35.9	10000
70	0.35,1	40,60	119,144	5000,10000
72	1,3	40	2.2–35.9	1000–10000
76	0.35,1	40,60,90	35.9–119	100,10000
77	1,3	40,60	35.9–72	2500, 10000
78	3	40,60	35.9,72	2500,10000
82	1,3	60,90	18–72	100–10000
84	1,3	60	70.7,72	10000
85	1,3	40	2.2,35.9	1000,10000
88	0.35,3	60,90	72,120	10000
93	0.35,1	40,60	35.4–72	10000
94	1,3	40	35.4,35.9	10000
98	1,3	40,60	4.5–35.4	2500,10000
100	3	60,90	2.2–6.7	100
103	1,3	40,60,90	2.2–70.7	100–10000
110	0.35,1	40,60,90	35.4–144	1000,10000
114	3	40	17.9	2500
115	3	40,60	2.2–72	1000,10000
120	1,3	40	2.2–9	1000,2500
121	1,3	40,60	9–35.9	5000
122	0.35,3	40,60	35.9–120	5000,10000
124	1,3	40	17.9,35.9	7500,10000
125	3	60	2.2,4.5	100
126	0.35,1	40,60,90	4.5–17.9	100
134	1,3	40,60	70.7,72	10000
137	1,3	40	17.9–72	1000,10000
138	1,3	40	35.9–72	1000,10000
140	1,3	40,60	9–70.7	1000–10000
141	0.35,1	40,60	2.2–35.9	100–10000
144	3	40,60	2.2	100
146	1,3	40	4.5–35.9	1000,10000
147	3	40	17.9,35.9	2500
149	1,3	40	6.7–35.9	1000–10000
150	1,3	60	17.9,35.9	7500,10000
152	1,3	40,60	70.7,72	10000
155	0.35,1	40,60,90	2.2–6.7	100
158	0.35,3	40,60	35.9,72	2500–10000
172	0.35	40,60,90	144	2500

where the 160 μm detection could either reside on the peak or form part of the rising continuum (e.g. see objects 115, 147, 152).

4 SED CHARACTERISATION

4.1 The Infrared Energy Budget

With the aid of the best-matched SK07 templates, we perform K-corrections and estimate the monochromatic rest frame luminosities at 24, 70 and 160 μm . In addition, by

integrating the SEDs between 8–1000 μm , we arrive at an array of values for the total infrared luminosity (L_{IR}) for each object, the average of which is then used as a final estimate. The sources in the redshift sample are categorised into luminosity classes, following the definition in Sanders & Mirabel (1996), revealing that it consists of 12 per cent Starbursts, 62 per cent LIRGs and 26 per cent ULIRGs. Despite the uncertainties on L_{IR} being relatively large and stemming from the lack of photometry longward of 160 μm , only two objects move to a different luminosity class on account of this (table 3).

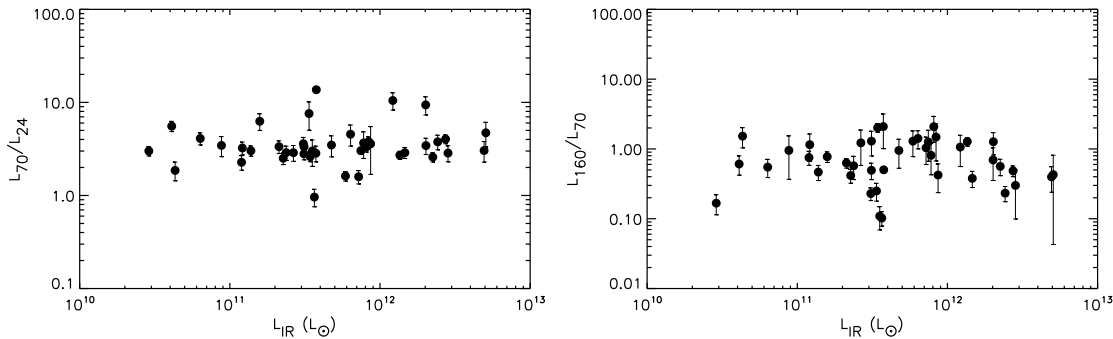


Figure 7. The K-corrected, rest frame luminosity ratios L_{70}/L_{24} , L_{160}/L_{70} as a function of the total infrared luminosity. All units are L_{\odot} and the 1σ uncertainties are shown.

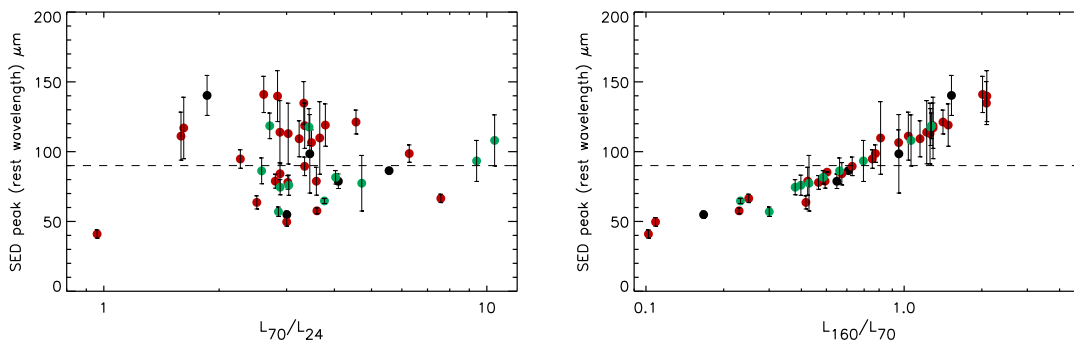


Figure 8. The position of the rest frame SED peak (in μm) as a function of the K-corrected, rest frame L_{70}/L_{24} ratio (left panel) and L_{160}/L_{70} ratio (right panel). L_{24} , L_{70} and L_{160} are in units of L_{\odot} and the 1σ uncertainties are shown. The colours correspond to the luminosity class: black for Starbursts, red for LIRGs and green for ULIRGs.

4.2 The mid-IR continuum slope and SED peak

Conventional methods of characterising infrared galaxies include associating flux ratios between various bands to physical processes responsible for emission in the infrared (e.g. Xu et al. 2001; Egami et al. 2004; Lutz et al. 2005; Verma et al. 2005). In particular, the f_{25}/f_{60} parameter has been applied extensively in *IRAS* studies of such systems, to quantify relative AGN/starburst contributions with an indicative value of $f_{25}/f_{60} > 0.17$ for AGN-dominated sources (e.g. de Grijp et al. 1985, Miley et al. 1985, Soifer et al. 1989). This ‘warm/cold’ terminology is based on the implication that dust heated by an AGN would reach higher temperatures and hence lower the continuum slope between 25 and 60 μm (or 24 and 70 μm in *Spitzer*’s case) (e.g. Farrah et al. 2005; Verma et al. 2005, Frayer et al. 2006). Calculating the 25/60 μm continuum slope using the model SEDs, reveals that for ~ 25 per cent of our sample the classical IRAS warm source criterion of $f_{25}/f_{60} > 0.17$ applies. However, the majority of these objects peak at $\lambda > 100 \mu\text{m}$, indicating that the flatter behaviour between 25 and 60 μm is due to a shift in infrared emission with elevated $\lambda > 90 \mu\text{m}$ flux and reduced 60 μm flux. Furthermore, from figure 7, it is clear that the continuum slope throughout the SED is completely independent from the total infrared luminosity. Consequently, if it is true that the contribution of AGN-dominated objects increases as a function of IR luminosity (e.g. Brand et al. 2006), then the slope of the mid-IR continuum and

hence the L_{70}/L_{24} ratio, fail to quantify it. In addition, because of heavy obscuration, emission from cool dust seems to be altering the mid-IR continuum slope solely due to increased far-IR emission. Various authors have supported this idea; Chakrabarti et al. (2007) have modelled infrared SEDs with varied starburst/AGN contributions, suggesting that the warm/cold classification of LIRGs/ULIRGs would be independent of the energy source, if sufficiently obscured so that all the far-IR emission comes from large grains in equilibrium. Similar observations (e.g. Lutz et al. 1996, Klaas et al. 1997) have put forward the notion that elevated optical extinction can be responsible for a steep rise of the mid-IR continuum and hence can displace the ratio of the ‘cold-warm’ components, resulting in an energy output mainly carried by the cold component.

To further investigate the properties of this sample, the wavelength at which the SEDs turn over into the Rayleigh-Jean regime is estimated (table 3, column 8). We find that a significant fraction of objects (40-60 per cent within 1σ) peak at wavelengths longward of 90 μm independent of luminosity class. Despite the large uncertainties, there is clearly a strong correlation with respect to L_{160}/L_{70} , not surprising, since 70 and 160 μm sample either side of the peak and their ratio is directly related to the far-IR turnover (figure 8, right panel). The same does not apply for the L_{70}/L_{24} ratio, however, which shows no such dependence (figure 8, left panel).

Table 3. The infrared budget and SED characteristics of the redshift sample. Column 1 classifies the objects according to their luminosity. Columns 2 and 3 are the Object ID and redshift, columns 4 and 5 are the K-corrected, rest-frame L_{70}/L_{24} and L_{160}/L_{70} ratios. Columns 6 and 7 quote the average value of the total infrared luminosity L_{IR} (in units of $\times 10^{10} L_{\odot}$) and its logarithm. The position of the far-IR turnover is displayed in column 8. All uncertainties are 1σ .

Type	ID	L_{70}/L_{24}	L_{160}/L_{70}	$L_{IR} \times 10^{10} (L_{\odot})$	$\log L_{IR}$	peak (rest, μm)
SBs	51	1.86	1.52	4.32 ± 0.23	10.64	140 ± 14
	155	3.00	0.17	2.89 ± 0.2	10.46	55 ± 2
	125	4.10	0.55	6.35 ± 0.72	10.81	79 ± 5
	144	5.56	0.61	4.10 ± 0.49	10.61	86 ± 2
SB/LIRG	103	3.45	0.95	8.79 ± 1.31	10.94	98 ± 28
LIRGs	141	0.96	0.10	36.54 ± 1.66	11.56	41 ± 3
	121	1.59	1.04	72.07 ± 8.26	11.86	111 ± 17
	150	1.62	1.29	58.88 ± 9.01	11.77	117 ± 22
	98	2.27	0.75	11.97 ± 1.0	11.08	95 ± 7
	100	2.51	0.42	22.68 ± 1.48	11.36	64 ± 5
	78	2.62	2.01	34.27 ± 1.03	11.53	141 ± 13
	120	2.80	0.49	31.15 ± 2.84	11.49	78 ± 5
	152	2.84	2.09	37.41 ± 8.58	11.57	140 ± 18
	115	2.88	1.22	26.50 ± 7.93	11.42	114 ± 23
	85	2.88	0.57	23.73 ± 2.32	11.37	84 ± 8
	76	3.00	0.11	35.41 ± 3.65	11.55	50 ± 3
	72	3.02	0.47	13.81 ± 0.87	11.14	78 ± 5
	147	3.03	1.26	74.57 ± 16.67	11.87	113 ± 22
	122	3.24	1.15	12.11 ± 2.31	11.08	109 ± 13
	77	3.33	2.08	81.11 ± 16.14	11.91	135 ± 15
	146	3.34	0.63	21.24 ± 0.98	11.33	90 ± 7
	140	3.35	1.29	31.18 ± 4.74	11.49	119 ± 16
	149	3.48	0.95	47.50 ± 7.27	11.68	107 ± 9
	55	3.59	0.42	86.61 ± 3.77	11.94	79 ± 10
	126	3.60	0.23	30.87 ± 1.90	11.49	58 ± 2
41	3.66	0.81	77.76 ± 8.38	11.89	110 ± 26	
137	4.55	1.41	63.65 ± 4.0	11.80	121 ± 8	
138	6.27	0.77	15.82 ± 0.59	11.20	99 ± 6	
110	7.58	0.25	33.68 ± 3.37	11.53	67 ± 3	
172	13.69	0.50	37.65 ± 0.12	11.58	85 ± 0	
(U)LIRG	134	3.79	1.48	83.94 ± 21.39	11.92	119 ± 15
ULIRGs	67	2.58	0.56	224.71 ± 2.74	12.35	86 ± 9
	114	2.71	1.27	135.64 ± 1.54	12.13	119 ± 9
	82	2.86	0.30	283.69 ± 39.97	12.45	57 ± 3
	124	2.89	0.38	146.39 ± 8.87	12.17	75 ± 5
	93	3.04	0.40	493.36 ± 55.53	12.69	76 ± 7
	84	3.43	1.27	202.19 ± 8.25	12.31	118 ± 13
	88	3.77	0.23	242.27 ± 15.29	12.38	65 ± 2
	94	4.03	0.49	273.44 ± 2.96	12.44	82 ± 5
	158	4.71	0.43	506.70 ± 111.65	12.70	77 ± 20
	70	9.40	0.69	201.46 ± 27.19	12.30	93 ± 15
58	10.48	1.06	121.73 ± 16.74	12.08	108 ± 18	

Figures 7 and 8 display some important properties of the sample, consistent with conclusions from section 3. Generally, a simple black body spectrum displays a temperature dependence through the position of the emission peak, the continuum slope and the total luminosity. Consequently, if the far-IR part of an SED were well-represented by a [modified] black body, for a sample of galaxies of varying dust temperatures this would manifest itself as: a) a positive correlation between mid-IR continuum slope and total infrared luminosity (as they both increase with temperature) and b) a negative correlation between mid-IR continuum slope and position of SED peak (as the former increases and the lat-

ter decreases with temperature). However, if an extra cold dust component is present, as we believe the case to be for the $70 \mu\text{m}$ sample, a *single* temperature black body is not a sufficiently accurate representation of the far-IR and these correlations would not apply. This is what is observed in figures 7 and 8.

5 EQUATIONS FOR ESTIMATING THE TOTAL INFRARED LUMINOSITY

Determining the infrared energy budget is crucial for estimating the contribution to the infrared and submillimetre

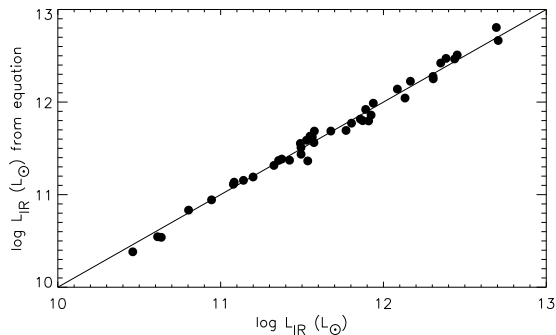


Figure 9. The relation between L_{IR} calculated using equation 1 (y-axis) and L_{IR} calculated by integrating under the SEDs (x-axis). The solid line has a gradient of 1. The r.m.s. scatter off the line is 0.06 dex.

backgrounds and plays an important role in establishing a value for the infrared element of the cosmic star formation history. If the available photometric data is not sufficient and hence unable to explicitly define these contributions, a first order approximation of the infrared energy budget can be attained through equations relating the total infrared luminosity to the monochromatic luminosity in one or more bands. In this section, we develop equations that can be used to estimate L_{IR} , using 1 or more MIPS bands. However, note that all have been derived using the typical form of starburst-type SEDs and have not been tested on power-law SEDs of AGN-dominated sources.

5.1 Estimating L_{IR} with all 3 MIPS bands

As the SED of an infrared-luminous galaxy has a distinct shape, its bolometric output can be approximated by summing contributions from four main sections: $< 24 \mu\text{m}$, $24\text{--}70 \mu\text{m}$, $70\text{--}160 \mu\text{m}$ and $> 160 \mu\text{m}$. In a linear plot of f_ν versus ν , flux shortward of $24 \mu\text{m}$ and longward of $160 \mu\text{m}$ is not as significant as the flux within that range. Therefore the $< 24 \mu\text{m}$ and $> 160 \mu\text{m}$ sections can be approximated by triangles of heights L_{24} and L_{160} and the sections within $24\text{--}160 \mu\text{m}$ with trapezia of heights of L_{24} , L_{70} and L_{160} . Summing these contributions and empirically accounting for the systematic offset in this approximation, we derive an equation to calculate the total infrared luminosity (L_{IR}) in the range $8\text{--}1000 \mu\text{m}$:

$$L_{IR} = 4.63 \times 10^{-15} \times (8.3L_{24} + 2.7L_{70} + L_{160}) \times (1+z). \quad (1)$$

The coefficients represent the width ($\Delta\nu$) of the bases of the sections in units of Hz, L_{IR} is in units of L_\odot and L_{24} , L_{70} and L_{160} are the monochromatic luminosity densities (in units of W/Hz) directly derived from the observed flux densities, without applying K-corrections. The factor $(1+z)$ adjusts the bases $\Delta\nu$ of the SED sections, as their width increases with redshift.

The validity of this method is demonstrated by comparing the value of L_{IR} derived by using the equation (y-axis) and the average value of L_{IR} derived by integrating under the best-matched model SEDs (x-axis) (figure 9). There is very good agreement, with an r.m.s. deviation of 0.06 dex from the true L_{IR} . We also test it on a different galaxy

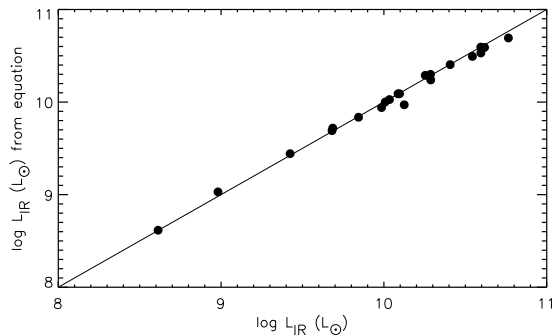


Figure 10. The relation between L_{IR} calculated using equation 1 (y-axis) and L_{IR} calculated by integrating under the SEDs (x-axis) for 21 SINGS galaxies. The solid line has a gradient of 1. The r.m.s. scatter off the line is 0.05 dex.

sample, by calculating the total infrared luminosity of 21 local infrared star-forming/starburst galaxies using MIPS photometry from the *Spitzer* Infrared Nearby Galaxy Survey (SINGS) (Dale et al. 2005, hereafter D05) and estimated distances quoted in Sanders et al. (2003). We fit the DH02 models on the 24 , 70 and $160 \mu\text{m}$ photometry (like in D05) and integrate under the $8\text{--}1000 \mu\text{m}$ region of the best-fit curve, comparing the result with L_{IR} from equation 1. The agreement is very good, with an r.m.s. scatter of 0.05 (figure 10), confirming that this equation is not specific to high- z LIRGs/ULIRGs, but also applicable to normal infrared star-forming galaxies in the local universe.

5.2 Estimating L_{IR} with 1 MIPS band

Naturally, a more luminous galaxy will also display higher luminosity at the various infrared photometric bands (e.g. Elbaz et al. 2002, Takeuchi et al. 2005). This would manifest itself as a strong positive correlation between L_{IR} and K-corrected rest-frame monochromatic luminosity at 24 , 70 and $160 \mu\text{m}$ (figure 11). As a result, it could be used instead of equation 1, for estimating L_{IR} , in cases where only one photometric data point from MIPS is available. For each plot in figure 11, we compute the least squares best fit line through the data, equations 2–4:

$$\log L_{IR} = 1.95 + 0.89 \log L_{24}, \quad (2)$$

$$\log L_{IR} = 1.16 + 0.92 \log L_{70}, \quad (3)$$

$$\log L_{IR} = 1.49 + 0.9 \log L_{160}, \quad (4)$$

All luminosities are in units of L_\odot and L_{24} , L_{70} and L_{160} are in the rest frame. The r.m.s. offsets from the best line fits are 0.18, 0.11, 0.23 dex for equations 2, 3 and 4 respectively. This intrinsic dispersion most likely stems from the variation in the properties of each galaxy, the high photometric uncertainties as well as the range of models used to calculate each luminosity value; nevertheless, they are convenient in cases where the luminosity of a galaxy is required only within an order of magnitude or class.

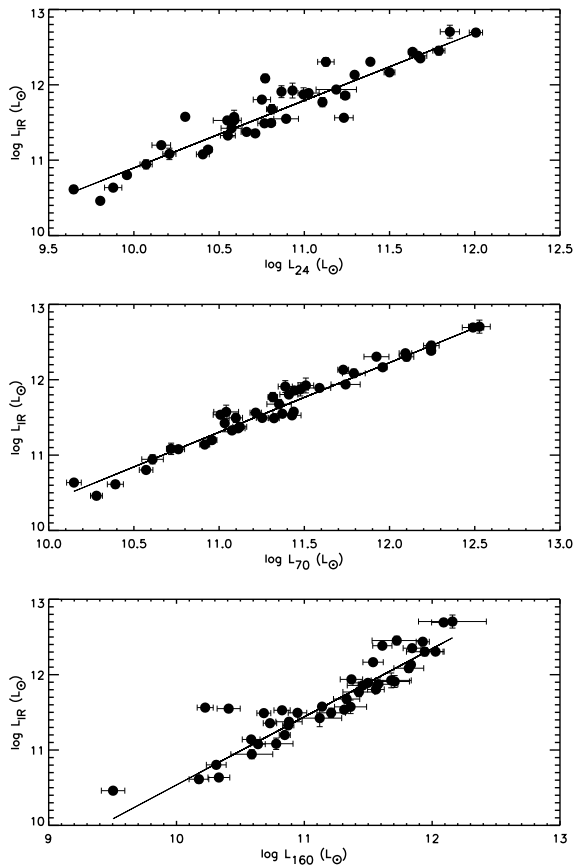


Figure 11. The monochromatic rest frame luminosity at 24, 70 and $160\ \mu\text{m}$ as a function of the total infrared luminosity for the redshift sample. The 1σ uncertainties are shown. The r.m.s. scatter is 0.18, 0.11, and 0.23 dex respectively.

6 SUMMARY AND CONCLUSION

We have examined a population of $70\ \mu\text{m}$ selected sources, in the region of the Extended Groth Strip, focusing this study on the infrared properties of 43 objects with available spectroscopic redshifts ($0.1 < z < 1.2$). In the last section, we derived a set of equations in order to estimate the total IR luminosity with at least one MIPS band, applicable to objects with starburst-type SEDs. We would like to emphasise that our selection criteria did not photometrically bias the redshift sample with respect to the full sample or predispose our study to a particular type of galaxy. As this is a flux limited survey (see section 2), the higher redshift objects are also more luminous in the infrared and display lower optical flux. This implies that the sources with no available spectroscopic redshift are also in the LIRG/ULIRG regime. In addition, the MIPS colours (figure 1) and SEDs (figure 2) unanimously show that all objects are photometrically similar in the mid and far-IR and their properties diverge only in the optical and near-IR, not relevant for the work described here.

By fitting 4 libraries of SED templates on our infrared photometry, we have examined the properties of the sources and estimated the infrared energy budget, revealing 12 per cent starbursts, 62 per cent LIRGs and 26 per cent ULIRGs. Evaluation of the fits showed that the SK07 models perform

better at reproducing the far-IR SED; their formulation adopts a two-component configuration of dust heated in the immediate locality of massive young stars and cirrus-heated dust, essentially decoupling mid and far infrared emission. As a result, since the total infrared luminosity is not directly related to the position of the SED peak or the steepness of the mid-IR continuum slope, with the SK07 templates it is possible to represent objects with strong mid-IR emission and an additional cold component. CE01 and DH02 employ a scenario with a single radiating central source where temperature varies as a function of distance from the centre. Although this has worked well with local infrared galaxies, it completely underestimates our sources' $160\ \mu\text{m}$ flux, with a discrepancy of at least a factor of 2 and up to 10 for extreme cases, since it does not allow for types of systems with elevated far-IR emission. Our empirical local galaxy templates, also mostly underestimate the far-IR region, indicative of the fact that an average dust temperature of 30-50 K is too high.

Considering all above points, we propose that this deep $70\ \mu\text{m}$ survey has probed high- z LIRGs and ULIRGs, which are unlike local counterparts: heavy obscuration and large amounts of cold dust potentially lower than 30 K, appear as a *far-infrared excess* component in the SEDs, causing a significant fraction to peak at $\lambda > 90\ \mu\text{m}$ and steepening the continuum slope. The existence of such objects has also been put forward by other authors; e.g. Marcellac et al. (2006) have suggested that some high- z infrared-luminous objects display far-IR properties divergent from those of local galaxies because of an additional cold dust component, even if the strength of mid-IR emission is the same. This has further implications: in such systems, the continuum slope cannot be representative of various galaxy characteristics such as dust temperature, total infrared luminosity or the nature of the central energy source. Figures 7 and 8 demonstrate this: the mid-IR continuum slope (quantified by the L_{70}/L_{24} ratio) satisfies the IRAS warm source criterion of $f_{25}/f_{60} > 0.17$ for sources with reduced $60\ \mu\text{m}$ emission and increased $\lambda > 90\ \mu\text{m}$ flux, as opposed to elevated $25\ \mu\text{m}$ emission and it is completely dissociated from the position of the SED turnover and total infrared luminosity. As this is inconsistent with the representation of far-IR emission as a single temperature black body, it is in line with our earlier suggestion of the presence of an additional cold emissive component.

It is worth noting that this $70\ \mu\text{m}$ sample is one of the first far-IR-selected samples reaching such low flux-density limits and additional similar surveys will be of great importance in highlighting the differences (if any) between local and high redshift infrared populations. The next infrared observatory, *Herschel*, will greatly benefit this work, extending to the sub-mm part of the spectrum and, hence, enabling a complete census of high- z infrared galaxy SEDs. Finally, we would like to mention that in order to confirm our conclusions we have planned a follow-up of the work described in this paper with submillimetre observations using the Submillimetre Common-User Bolometer Array (SCUBA 2).

ACKNOWLEDGMENTS

M.S. has received support from the University of Oxford, department of Astrophysics. This work is based on observations made with the Spitzer Space Telescope, operated by the Jet Propulsion Laboratory, California Institute of Technology, under NASA contract 1407. We thank Pat Roche, Aprajita Verma, Steve Rawlings and Tom Mauch for useful discussions and comments.

REFERENCES

Alonso-Herrero, A. et al., 2001, ApJ, 121, 1369-1384
Alonso-Herrero, A. et al., 2006, ApJ, 640, 167-184
Appleton, P., N. et al., 2004, ApJS, 154, 147-150
Armus, L. et al., 2007, ApJ, 656, 148-167
Brand, K. et al., 2006, ApJ, 644, 143-147
Brandl, B., R. et al., 2006, ApJ, 653, 1129-1144
Calzetti, D. et al. 2000, ApJ, 533, 682
Chakrabarti, S. et al., ApJ, 2007, 658, 840
Chary, R. & Elbaz, D., 2001, ApJ, 556, 562
Dale, D., A. et al. 2005, ApJ, 633, 857
Dale, D., A. & Helou, G., 2002, ApJ, 576, 159-168
Davis, M. et al. 2003, SPIE, 4834, 161
Davis, M. et al. 2007, ApJ, 660, 1-6
Desert, F.-X., Boulanger, F. & Puget, J. L., 1990, A&A, 237, 215-236
Dunne, L. et al., 2000, MNRAS, 315, 115
Efstathiou, G. & Rowan-Robinson, M., 1990, MNRAS, 245, 275
Efstathiou, A., Rowan-Robinson, M. & Siebenmorgen, R., 2000, MNRAS, 313, 734
Egami, E. et al. 2004, ApJS, 154, 130
Elbaz, D. et al., 2002, A&A 384, 848-865
Farrah, D. et al. 2003, MNRAS, 343, 585
Farrah, D. et al. 2005, ApJ, 626, 70
Franceschini, A. et al. 2001, A&A, 378, 1
Frayser, D., T. et al. 2006, AJ, 131, 250
Genzel, R. et al., 1998, ApJ, 498, 579
Granato, G. L. & Danese, L., 1994, MNRAS, 268, 235
de Grijp, M. H. K. et al. 1985, Natur, 314, 240
Gregorich, D., T. et al. 1995, AJ, 110, 259
Guideroni, B. et al. 1998, MNRAS, 295, 877
Hao et al. 2007, ApJ, 655, 77
Holland, W. et al., 2006, SPIE, 6275E, 45H
Klaas, U. et al. 1997, A&A, 325, 21
Klaas, U. et al. 2001, A&A, 379, 823
Krügel, E. & Siebenmorgen, R., 1994, A&A, 282, 407
Lacy, M. et al. 2004, ApJS, 154, 166
Lançon et al., 1996, A&ASS, 115, 253-265
Lisenfeld, U., Isaak, K., G. & Hills, R., 2000, MNRAS, 312, 433
Lu, N., et al., 2003, ApJ, 588, 199-217
Lutz, D. et al. 1996, A&A, 315, 137
Lutz, D. et al. 2005, ApJ, 632, 13
Marcillac, D. et al., 2006, A&A, 451, 57
Miley, G., K. et al., 1985, ApJ, 293, 11
Mitchell, R. M. & Robinson, G., 1981, MNRAS, 196, 801
Rigopoulou, D. et al., 1999, AJ, 118, 2625
Rowan-Robinson, M., 1980, ApJS, 44, 403
Rowan-Robinson, M., 1995, MNRAS, 272, 737
Rowan-Robinson, M., 2000, MNRAS, 316, 885
Rowan-Robinson, M. et al., 2005, AJ, 129, 1183
Sanders, D., B. et al., 1987, ApJ, 312, 5
Sanders, D., B. et al., 1988, ApJ, 325, 74
Sanders D., B., et al., 1989, ApJ, 347, 29
Sanders, D., B. & Mirabel, I., F., 1996, ARA&A, 34, 749
Sanders, D., B. et al., 2003, AJ, 126, 1607
Siebenmorgen, R. & Krügel, E., 2007, A&A, 461, 445
Silva, L. et al. 1998, ApJ, 509, 103-117
Smith, B., J. et al. 1987, ApJ, 318, 161
Soifer, B., T. et al., 1986, ApJ, 303, 41
Soifer, B., T. et al. 1989, AJ, 98, 766
Stern, D. et al. 2005, ApJ, 631, 163
Symeonidis, M. et al. 2007, ApJ, 660, 73
Tacconi, L., J. et al. 2002, ApJ, 580, 73
Takeuchi, T., T. et al. 2005, A&A, 432, 423
Tran, Q., D. et al. 2001, ApJ, 552, 527
Veilleux, S. et al. 1997, ApJ, 484, 92
Verma, A. et al. 2005, SSRv, 119, 355
Ward, M. et al., ApJ, 1987, 315, 74
Xu, C. et al. 2001, ApJ, 562, 179